Computer Modeling in
Engineering & Sciences

Tech Science Press

https://doi.org/10.32604/cmes.2026.086426

ARTICLE

Interpretable Machine-Learning Prediction of Seismic Performance of Earthquake-Damaged CFRP-Repaired Hollow Bridge Piers

Fengqi Guo[1,2], Song Tan[1], Liqiang Jiang[1,2,*], Wei Guo[1,2] and Lizhong Jiang[1,2]

[1]School of Civil Engineering, Central South University, Changsha, China
[2]National Engineering Laboratory for High-Speed Railway Construction, Changsha, China

*Corresponding Author: Liqiang Jiang. Email: jianglq2019@csu.edu.cn

Received: 30 May 2026; Accepted: 05 August 2026; Published: 28 August 2026

ABSTRACT: Rapid post-earthquake recovery of high-speed railway bridges requires practical tools for evaluating repaired seismic performance across multiple indicators, rather than peak strength alone. This study develops a target-wise machine-learning framework for rapid multi-indicator prediction of the seismic performance of earthquake-damaged hollow bridge piers repaired with carbon fiber-reinforced polymer (CFRP). An OpenSeesPy-based finite-element model was first validated against test results previously reported by the authors and then used to generate a numerical database covering different loading directions, pre-repair damage states and CFRP repair configurations. Four performance indicators were extracted from the simulated cyclic responses: peak lateral strength, equivalent viscous damping ratio, re-centering indicator and stiffness degradation indicator. Seven nonlinear regression algorithms were compared separately for each performance target using a predefined five-fold cross-validation protocol. The selected estimators were retained in a common four-model predictor bank comprising independently trained target-specific models. The results show that CatBoost was selected for peak lateral strength and achieved an independent-test coefficient of determination (R^2) of 0.9981. Support vector regression (SVR) with a radial basis function (RBF) kernel was selected for the equivalent viscous damping ratio, re-centering indicator and stiffness degradation indicator, with R^2 values of 0.9666, 0.9548 and 0.9625, respectively. Several alternative models nevertheless achieved closely comparable accuracy for the latter three indicators. Grouped error analysis showed low percentage errors across the damage-state and loading-direction subsets, although prediction performance varied among several direction–indicator combinations. Model-agnostic interpretability analysis further revealed distinct target-specific attribution patterns for damage state, loading direction, and CFRP parameters across the four performance indicators. These findings demonstrate that target-specific surrogate modelling can capture the coupled but non-identical responses governing repaired seismic performance and can support rapid preliminary screening of CFRP repair schemes within the sampled numerical response domain.

KEYWORDS: Earthquake-damaged CFRP repair; hollow bridge piers; machine learning; finite element simulation

1 Introduction

Post-earthquake bridge management increasingly requires rapid identification of repairable components and reliable estimation of residual serviceability, rather than only collapse prevention. For reinforced-concrete bridge columns, this shift changes the central assessment question from whether a member has survived an earthquake to how much usable seismic function remains after damage and repair. Review studies on seismic repair of reinforced-concrete bridge columns show that repair decisions depend on damage extent, residual deformation, repairability and restored cyclic capacity, not on strength recovery alone [1]. Recent work on post-earthquake serviceability assessment has also shown the need to connect observable damage, analytical response and serviceability judgement in time-sensitive bridge management [2]. This requirement is particularly important for high-speed railway bridge systems, where prolonged interruption can have network-level consequences [3,4]. In this context, a repair-assessment framework should define a repairable response domain and estimate multiple residual or repaired performance quantities within that domain, instead of reducing post-earthquake recovery to a single scalar target.

Round-ended hollow reinforced-concrete bridge piers pose a specific challenge because their seismic response is controlled by geometry, loading direction and damage localisation. The hollow section, curved end regions and web-wall configuration can lead to non-uniform stress transfer and direction-dependent plastic development. Experimental and numerical studies on round-end hollow reinforced-concrete bridge piers have reported complex damage ranges and higher-mode response effects that are not fully represented by simplified solid-column assumptions [5]. Plastic hinge investigations for round-ended hollow columns further indicate that the damage-critical region depends on section form, variable geometry and cyclic demand [6]. For earthquake-damaged round-ended hollow piers, the repair problem therefore involves not only restoring lateral resistance, but also accounting for residual deformation, stiffness degradation and loading-direction sensitivity.

Carbon fiber-reinforced polymer (CFRP) and other fiber-reinforced polymer (FRP) repair methods provide a practical way to recover part of the seismic function of damaged reinforced-concrete columns, but their effects are not uniform across all performance indicators. Recent experiments on damaged resilient reinforced-concrete columns retrofitted with FRP sheets show that repaired strength, residual deformation, stiffness and energy-dissipation characteristics may evolve differently after intervention [7]. CFRP bars and sheets have also been used for seismic repair of damaged columns, confirming the repair potential of CFRP-based systems while showing that the repaired cyclic response remains damage-state dependent [8]. For damping-related behaviour, tests on repaired and strengthened reinforced-concrete columns with CFRP jacketing under biaxial loading demonstrate that energy dissipation and equivalent viscous damping require direct evaluation, because they cannot be inferred reliably from strength enhancement alone [9]. Directional effects are also relevant for CFRP-retrofitted columns, especially under lateral loading in different directions or oblique earthquake actions [10,11]. These findings imply that CFRP wrapping may improve peak strength while producing different, and sometimes weaker, changes in equivalent damping, re-centering behaviour and stiffness degradation. A composite performance index can therefore obscure trade-offs among repaired engineering objectives.

Validated finite-element (FE) simulation and machine-learning (ML) surrogates offer a practical route for evaluating these coupled but non-identical repair responses. Once anchored to cyclic test evidence, a finite-element model can generate a broader repairable-response database than a limited experimental programme, covering damage states, loading directions and CFRP configurations that are difficult to test exhaustively. Machine-learning models can then approximate the finite-element-generated response at much lower computational cost. Recent reviews show that machine learning is increasingly used in earthquake-engineering performance evaluation and seismic design, but also stress the need for physically meaningful datasets and interpretable models [12]. Hybrid convolutional neural network (CNN)-LSTM and attention-based sequence models have further been used to predict bridge-pier hysteresis and backbone curves [13]. Physics-informed neural networks have also been introduced for advanced hysteretic modelling of reinforced-concrete structures under cyclic loads [14]. These approaches focus on complete hysteretic-loop or degradation-trajectory prediction. At the bridge-pier scale, data-driven methods have been used for seismic performance limit-state identification [15], and probabilistic learning has been applied to predict and correlate multiple seismic capacity measures of pier columns [16]. These studies support a multi-response view of seismic performance: correlated indicators may share mechanisms, but they are not interchangeable. Consequently, selecting one model form for all responses, or training a surrogate only for a single composite output, may hide target-specific behaviour. Explainable machine learning can help address this issue by checking whether influential variables and response trends are mechanically plausible rather than only statistically accurate [17,18]. In contrast, the present study focuses on a scalar-indicator surrogate task rather than full response-history prediction. The inputs are tabular descriptors of loading direction, damage state and CFRP repair parameters, and the outputs are repaired-performance indicators extracted from cyclic FE responses. Therefore, interpretable nonlinear regression models remain appropriate for rapid multi-indicator screening, target-wise comparison and mechanical interpretation.

However, existing data-driven prediction frameworks remain limited for repair-oriented assessment of earthquake-damaged bridge piers. Many studies focus on single response quantities, limit-state classification or general structural-response prediction. Such formulations do not fully address repaired components, for which strength recovery, energy dissipation, residual-deformation control and stiffness-degradation mitigation may evolve differently after CFRP intervention. Therefore, CFRP-repaired hollow bridge piers require a multi-indicator assessment framework rather than a strength-only or single-output prediction model. Because these indicators are physically correlated but not interchangeable, their trade-offs, mechanical consistency and applicability domain should be explicitly examined for engineering use.

To address these limitations, this study develops a repair-oriented multi-indicator FE-to-ML surrogate framework for CFRP-repaired, earthquake-damaged round-ended hollow bridge piers. The relevant quasi-static test results have already been reported in the authors' previous study [19]; therefore, the present paper uses those reported results only to validate the numerical model. The database is generated within the sampled finite-element response domain and covers loading direction, pre-repair damage state and CFRP repair parameters. Four repaired seismic-performance indicators are predicted separately: peak lateral strength $F_{\max}$, equivalent viscous damping ratio ξ_{eq}, re-centering indicator R_{recenter} and stiffness degradation indicator K_{stiff}. This indicator set preserves the trade-offs among strength recovery, equivalent damping, re-centering capacity and stiffness-degradation mitigation. Instead of imposing a single model or a single composite performance index, seven candidate regression algorithms are trained and selected independently for each target. The selected models are then evaluated through independent testing, grouped error analysis by damage state and loading direction, and model-agnostic interpretability analysis. The intended use of the framework is rapid preliminary screening and multi-indicator assessment of CFRP repair performance within the sampled numerical response domain, rather than direct field-level performance prediction or replacement of experimental validation.

The principal contributions of this study are threefold. First, it establishes an experimentally anchored FE database for multi-indicator assessment of earthquake-damaged, CFRP-repaired hollow bridge piers. Second, it develops a target-wise model-selection framework that preserves the distinct engineering meanings and trade-offs of the four performance indicators. Third, it combines independent testing, grouped error diagnostics, and model-agnostic interpretability analysis to assess predictive accuracy, local stability, and mechanical consistency within the sampled numerical response domain.

2 FE Model Development and Validation

OpenSeesPy Model and Validation

The quasi-static cyclic test results used for model validation were reported in the authors' previous study [19]. The experimental benchmark comprised four 1:10-scale round-ended hollow reinforced-concrete pier specimens. Specimens 1 and 2 were unrepaired reference specimens tested along the x and y principal directions, respectively, whereas Specimens 3 and 4 were the corresponding CFRP-repaired specimens tested along the same directions. All four specimens were subjected to uniaxial reversed cyclic loading along one principal lateral direction. The present study uses the published hysteresis curves and characteristic response quantities as validation evidence; complete specimen details and quantitative comparisons are available in Ref. [19].

Three types of numerical models, namely undamaged, damaged, and CFRP-repaired models, were developed in OpenSeesPy to reproduce the experimental response reported in the authors' previous study [19] and to generate numerical repair cases. The undamaged round-ended hollow reinforced-concrete pier was simulated using a fiber-section approach within the OpenSees framework [20–22]. The pier column was discretized into 12 nodes along the height, with nodes 2–5 covering the plastic-hinge region identified from the test damage pattern. To account for bond-slip and shear-related pinching that are difficult to capture with a standard fiber section, a calibrated zero-length spring using the Pinching4 material was placed between nodes 1 and 2. The remaining components were modelled using nonlinearBeamColumn elements, and cover concrete, core concrete, and longitudinal reinforcement were represented by the standard OpenSees Concrete01, Concrete02, and Steel02 material models [22].

The damaged model was constructed from the undamaged model by reducing the elastic moduli of the damaged materials to represent residual stiffness degradation [23,24]. This simplified damage representation does not explicitly resolve local concrete spalling or bar buckling, but it markedly reduces computational cost and is therefore suitable for the subsequent large-scale parametric analysis. The elastic moduli of steel and concrete were reduced using damage-state-dependent coefficients γ_r and γ_c, as listed in Table 1. The reduction coefficients were assigned from previous repaired-column modelling and experimental repair studies [23–25]. After repair, the core concrete in the plastic hinge region was not reduced [24], whereas the reduction coefficients for yielded and unyielded reinforcement were taken as 0.3 and 0.5, respectively [23].

Table 1: Elastic modulus reduction coefficients for material damage [23,24].

Damage State	**Damage State Description**	**Reinforcement Reduction Coefficient γ_r**	**Concrete Reduction Coefficient γ_c**
DS1	Concrete cracking	1.00	1.00
DS2	Slight concrete spalling or local cover loss	0.67	0.95
DS3	Multiple concrete cracks with evident spalling damage	0.50	0.90
DS4	Concrete spalling with exposed longitudinal bars or stirrups	0.30–0.40	0.85
DS5	Core concrete spalling with yielded longitudinal bars	0.20	0.80

The CFRP-repaired model was obtained by modifying the material properties in the plastic hinge region of the damaged model. To represent the confinement effect provided by CFRP wrapping, the cover concrete was modelled using a confined-concrete stress-strain relationship compatible with stirrup and FRP confinement [26]. In the OpenSeesPy implementation [22], an equivalent rectangular section was introduced only at the material level to define the confinement-enhanced concrete response of the round-ended hollow section. The structural fiber section retained the original round-ended hollow geometry. The equivalent section size was set to 823 mm by 443 mm as an area- and stiffness-consistent approximation for the confinement calculation, as shown in Fig. 1.

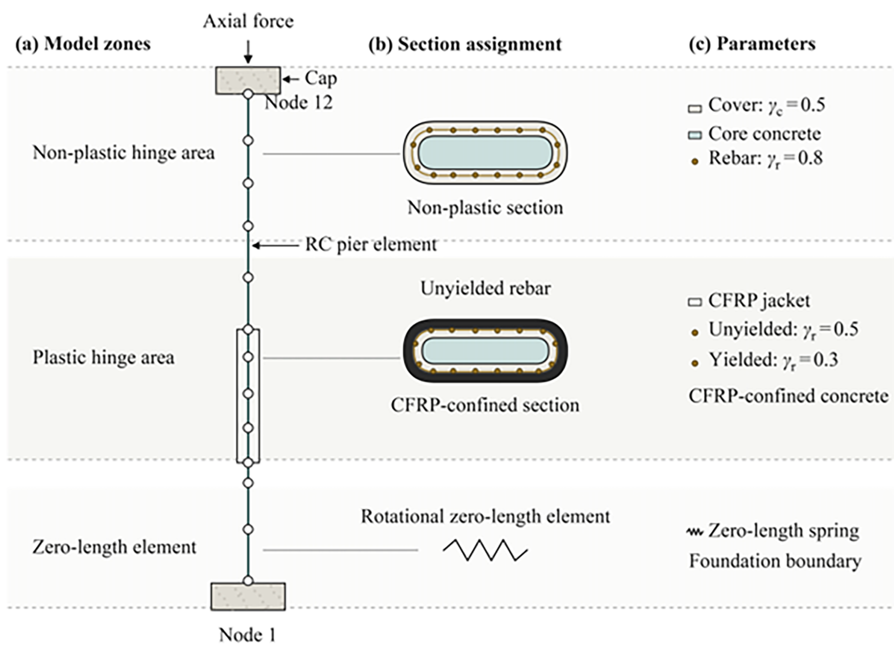

Figure 1: CFRP-repaired model.

The numerical models were compared with the experimental hysteresis curves reported in the authors' previous study [19], as shown in Fig. 2. The models reproduced the principal hysteretic characteristics and peak lateral strengths of the unrepaired and CFRP-repaired specimens. Across the positive- and negative-branch peak-load comparisons, the absolute relative differences between the FE predictions and experimental measurements ranged from 1.4% to approximately 20.0%. The complete specimen-level comparisons are reported in Ref. [19] and are not duplicated here. These discrepancies are treated as FE physical-modelling uncertainty rather than ML surrogate interpolation error. The FE model is therefore used as an experimentally anchored numerical model for repair-parameter trend analysis and response-database generation, not as an error-free representation of actual repaired-pier behaviour. Because the available validation tests involved uniaxial reversed cyclic loading along only the two principal directions, the present validation does not establish model accuracy under arbitrary oblique loading or simultaneous biaxial loading. These loading conditions remain outside the validated domain and require dedicated experimental or numerical assessment.

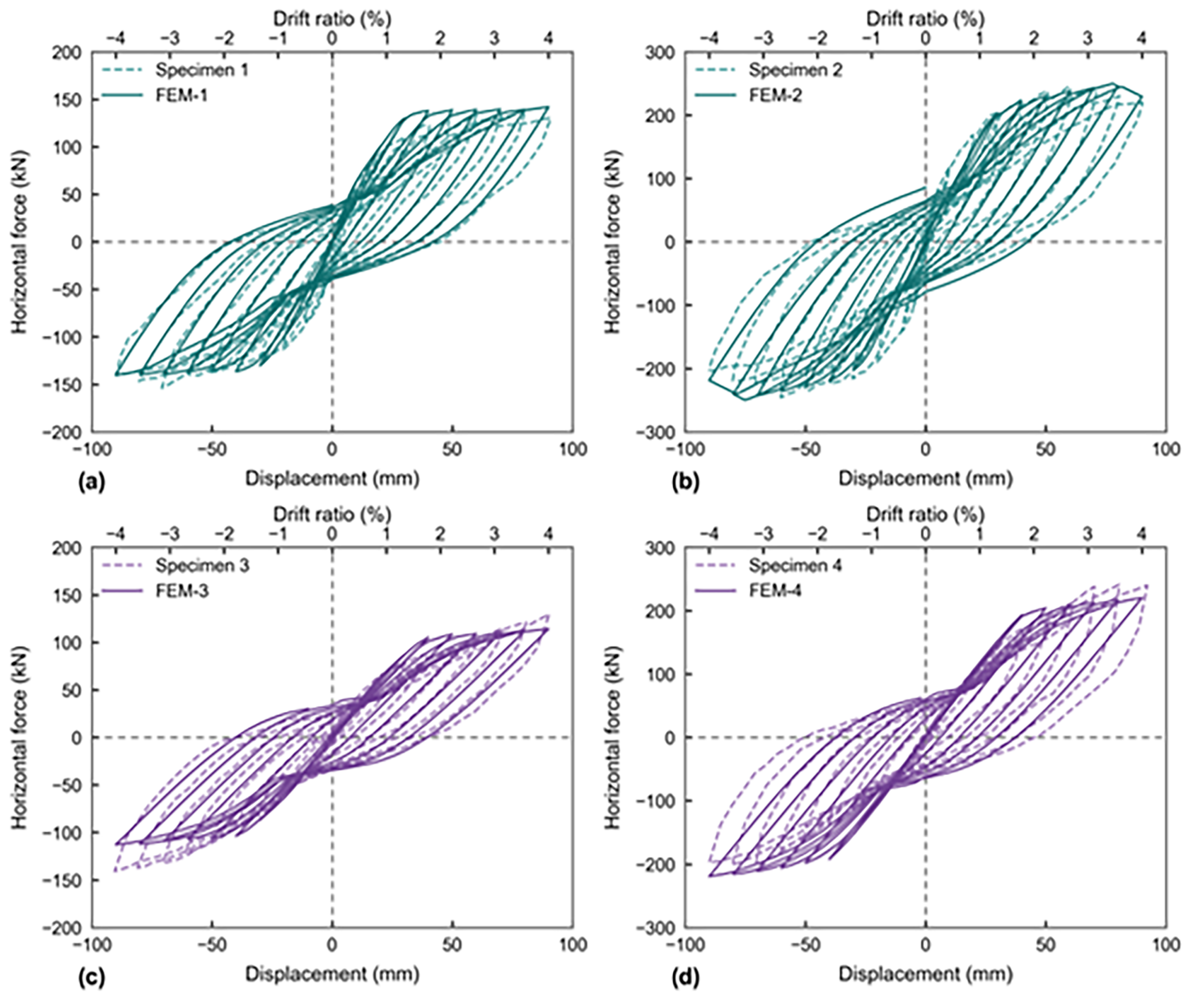

Figure 2: Comparison of experimental and numerical hysteresis responses: (**a**) Specimen 1–FEM-1, unrepaired, x direction; (**b**) Specimen 2–FEM-2, unrepaired, y direction; (**c**) Specimen 3–FEM-3, CFRP-repaired, x direction; and (**d**) Specimen 4–FEM-4, CFRP-repaired, y direction.

3 Simulation Database and Multi-Indicator Machine Learning Framework

3.1 Mathematical Formulation and Multi-Indicator Machine-Learning Framework

A target-wise supervised-regression framework was developed to map each repair-case description to four seismic-performance indicators. This formulation retains strength recovery, energy dissipation, residual-deformation control and stiffness degradation as separate prediction tasks rather than compressing them into a single score.

The input vector was defined as $\mathbf{X} = [\text{Direction}, DS, t_{\text{CFRP}}, n_{\text{CFRP}}, f_{\text{CFRP}}, E_{\text{CFRP}}, h_{\text{CFRP}}]$, where Direction denotes the lateral loading direction, DS denotes the pre-repair damage state and the remaining variables describe the CFRP repair configuration. The output vector was $\mathbf{Y} = \left[F_{\max}, \xi_{\text{eq}}, R_{\text{recenter}}, K_{\text{stiff}}\right]$. The set of prediction targets is defined as $\mathcal{Q} = \left\{F_{\max}, \xi_{\text{eq}}, R_{\text{recenter}}, K_{\text{stiff}}\right\}$. For each retained FE case, the target-specific prediction is defined as $\hat{y}_{i,q} = g_q\left(\mathbf{X}_i; \boldsymbol{\beta}_q\right), \quad q \in \mathcal{Q}$. The mapping function represents the estimator independently trained for each prediction target, and the associated parameter vector is target-specific. The common four-indicator inference interface is expressed as $\hat{\mathbf{Y}}_i = \mathcal{G}\left(\mathbf{X}_i; \mathcal{B}\right) = \left[g_q\left(\mathbf{X}_i; \boldsymbol{\beta}_q\right)\right]_{q \in \mathcal{Q}}$. The collection of the four target-specific parameter vectors is defined as $\mathcal{B} = \left\{\boldsymbol{\beta}_q : q \in \mathcal{Q}\right\}$. Each parameter vector is estimated independently for its corresponding target. Therefore, the common interface returns the four predicted indicators without sharing model parameters or latent representations. The machine-learning residual is defined as $\mathbf{e}_i^{\mathrm{ML}} = \mathbf{Y}_i^{\mathrm{FE}} - \hat{\mathbf{Y}}_i$. This residual quantifies the discrepancy between the surrogate predictions and the FE-generated labels. It does not represent the physical discrepancy between the FE model and experimental or field behaviour.

Fig. 3 summarises the workflow: panel a shows the target-wise supervised-regression protocol linking input variables and FE data to model selection and four-indicator inference using four independently trained target-specific models; panel b shows the candidate model pool and target-wise selection loop; and panel c shows the selected target-specific predictors and independent-test metrics.

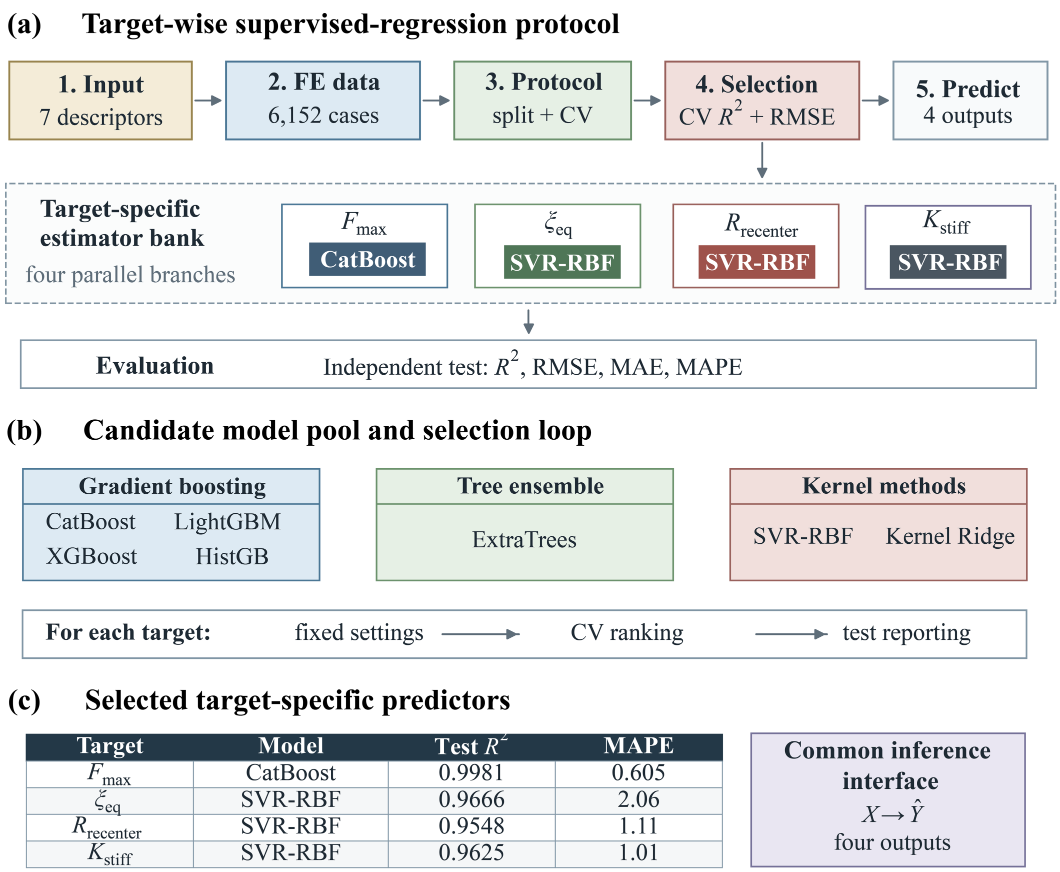

Figure 3: Proposed multi-indicator machine-learning framework: (**a**) target-wise prediction workflow; (**b**) candidate-model selection; (**c**) selected predictors and independent-test metrics.

All candidate algorithms used the same feature definition, train-test split, cross-validation procedure and independent-test protocol. To reduce composition bias in the main categorical response sources, the train-test split was stratified by damage state and loading direction. The same split was then used for all candidate algorithms and all response targets, so that the model comparison was not affected by different training-data compositions. The candidate pool comprised gradient-boosting models (CatBoost, XGBoost, LightGBM and HistGradientBoosting), a tree ensemble (ExtraTrees) and kernel methods, including support vector regression with a radial basis function kernel (SVR-RBF) and Kernel Ridge. Direction and damage state (DS) were one-hot encoded as categorical variables, and numerical repair variables were passed directly to tree-based models and standardised for kernel-based models [27–29]. The explicit data split, cross-validation, preprocessing and fixed model settings are summarised in Table 2.

Table 2: Machine-learning training and evaluation protocol.

Protocol Element	Implementation in this Study
Database screening	10,000 FE analyses attempted; 6152 valid cases retained (61.52%); 3848 cases excluded (38.48%) because no valid completed converged cycle was available for indicator extraction.
Dataset split	6152 converged FE cases; 80% training and 20% independent testing; stratified by loading direction and damage state; random_state = 42. The distributions of the continuous and integer-valued CFRP parameters were checked after splitting using their means, standard deviations, ranges, and absolute standardized mean differences.
Preprocessing	Direction and DS were one-hot encoded. Continuous repair variables were passed through for tree-based models and standardized for kernel-based models. For SVR-RBF and Kernel Ridge, the response target was also standardized within the fitted estimator pipeline.
Model selection	Seven regressors were compared using shuffled five-fold stratified cross-validation on the training subset; selection used the coefficient of determination (R^2) and RMSE.
Candidate regressors	CatBoost, XGBoost, LightGBM, HistGradientBoosting, ExtraTrees, SVR-RBF and Kernel Ridge.
Fixed hyperparameter configurations	CatBoost: iterations = 800, learning_rate = 0.05, depth = 6, loss_function = RMSE; LightGBM: n_estimators = 800, learning_rate = 0.03, num_leaves = 31, subsample = 0.85, colsample_bytree = 0.85, reg_lambda = 1.0; XGBoost: n_estimators = 800, learning_rate = 0.03, max_depth = 5, subsample = 0.85, colsample_bytree = 0.85, reg_lambda = 1.0, objective = reg:squarederror, tree_method = hist; ExtraTrees: n_estimators = 600, min_samples_leaf = 2; HistGradientBoosting: max_iter = 500, learning_rate = 0.05, l2_regularization = 0.01, early_stopping = True; SVR-RBF: C = 10.0, ε = 0.05, γ = scale; Kernel Ridge: kernel = RBF, α = 0.5, γ = 0.1. A random state of 42 was used where applicable.
Hyperparameter policy	The same configuration of each algorithm was applied to all four response targets. No exhaustive or target-specific hyperparameter search was conducted. The resulting ranking should therefore be interpreted as conditional on these predefined configurations.
Final evaluation	Independent-test metrics were not used for model ranking. They were reported for all candidate models and for the selected estimator bank using R^2, RMSE, mean absolute error (MAE), and mean absolute percentage error (MAPE).

Although the train–test split was stratified by damage state and loading direction, the distributions of the five CFRP parameters were checked after splitting using their means, standard deviations, ranges, and absolute standardized mean differences. The corresponding training/testing means were 0.469/0.482 mm for t_{CFRP}, 5.053/5.010 for n_{CFRP}, 3455/3398 MPa for f_{CFRP}, 224,027/223,512 MPa for E_{CFRP}, and 1.084/1.091 m for h_{CFRP}. The parameter ranges and standard deviations were also closely comparable between the two subsets. The absolute standardized mean differences were 0.045, 0.017, 0.066, 0.012, and 0.011, respectively. All values were below 0.07. These descriptive balance diagnostics indicate that the CFRP-parameter distributions were generally comparable between the training and testing subsets.

The seven regressors were evaluated using fixed, reproducible hyperparameter configurations under the same preprocessing, data-splitting, and five-fold cross-validation protocol. For each algorithm, the same configuration was applied to all four response targets and was fixed before model comparison. The objective was to establish a transparent model-family benchmark rather than to determine a globally optimized configuration for every model–target combination. Systematic optimization was not conducted because the seven algorithms involve heterogeneous hyperparameter spaces and search strategies, and a full nested optimization of all 28 model–target combinations was beyond the intended scope of the present study. Candidate models were ranked according to the mean cross-validation R^2, with the mean cross-validation root-mean-square error (RMSE) used as a secondary criterion. Independent-test metrics were excluded from the model-selection rule and were used only for subsequent performance reporting.

The final estimator for each response indicator was selected using five-fold stratified cross-validation on the training subset and was then evaluated on the independent test subset. The selected predictor bank identifies CatBoost for F_{max} and SVR-RBF for ξ_{eq}, R_{recenter} and K_{stiff}, showing that the selected regression form differed across outputs.

Each selected estimator was stored with its preprocessing pipeline, feature definition, target name and test-set metrics. The four estimator bundles can be queried individually or through the common inference interface defined above. This interface provides coordinated access to four independently trained target-specific estimators; it does not denote parameter sharing, a shared latent representation or a multi-task architecture.

The framework is intended for rapid post-repair performance prediction within the sampled repairable damage domain. Because the machine-learning models are trained using FE-generated labels, they should be interpreted as surrogate interpolators of the experimentally anchored numerical response space, rather than as predictors independently validated against actual repaired-pier behaviour. Accordingly, the proposed framework should be understood as an FE-to-ML surrogate modelling approach for preliminary comparison and parametric screening. It is not designed for automatic repair optimisation. It is also not intended to replace experimental validation, field-level performance assessment or final engineering judgement. Rather, it provides multi-indicator estimates for engineering judgement, sensitivity analysis and preliminary screening of CFRP repair schemes.

3.2 FE Simulation Database

The experimentally anchored FE model was used to construct a simulation database for multi-indicator machine-learning prediction. The simulations varied loading direction, damage state and CFRP repair parameters within the repairable damage domain. The input variables were loading direction (Direction), damage state (DS), nominal thickness of one CFRP layer (t_{CFRP}), number of CFRP layers (n_{CFRP}), tensile strength (f_{CFRP}), elastic modulus (E_{CFRP}) and repair height (h_{CFRP}).

A total of 10,000 FE analyses were attempted. Of these, 6152 analyses (61.52%) produced valid completed-cycle response records and were retained for model training and testing. The remaining 3848 analyses

(38.48%) did not provide a valid completed converged cycle for performance-indicator extraction and were therefore excluded. Using the input and output vector definitions introduced in Section 3.1, the retained FE dataset is represented as follows: $\mathcal{D}_{\mathrm{FE}} = \left\{\left(\mathbf{X}_i, \mathbf{Y}_i^{\mathrm{FE}}\right)\right\}_{i=1}^{N}, \quad N = 6152$. The case index spans the 6152 retained cases, whereas the 3848 excluded analyses are not elements of the machine-learning dataset. The retained cases were divided into 4921 training cases and 1231 independent-test cases. Cross-validation and model selection were conducted only within the training subset, whereas the independent-test subset was reserved for final performance evaluation.

Here, Direction represents only the x and y principal loading directions and does not encode arbitrary oblique angles or simultaneous biaxial loading paths. The retained database covers five damage states and two loading directions. All retained cases were generated from the same prototype pier geometry, axial-load condition, reinforcement configuration, and base concrete and reinforcement properties. Only loading direction, pre-repair damage state, CFRP thickness, number of CFRP layers, CFRP tensile strength, CFRP elastic modulus, and repair height were varied. Therefore, the increased number of retained cases expands the sampled parameter combinations within one fixed structural configuration but does not establish cross-pier generalisability. The sampled CFRP parameters span t_{CFRP} = 0.0502–1.0000 mm, n_{CFRP} = 1–10, f_{CFRP} = 2000–4999 MPa, E_{CFRP} = 150,016–299,986 MPa and h_{CFRP} = 0.043–2.150 m. The repair configuration tested in the authors' previous study used three CFRP layers, a total nominal thickness of 0.501 and a 600 mm wrapping height [19]. The wider sampling ranges should therefore be interpreted as a numerical extension of the FE formulation validated against those tests, rather than as fully experimentally verified repair configurations. The practical use of the database is limited to the sampled and converged numerical response domain. Inputs near the boundaries of the sampled CFRP ranges should be interpreted cautiously, whereas inputs outside these ranges or structural conditions beyond the investigated prototype should be treated as out of domain. Such cases require case-specific FE analysis and, where practicable, additional experimental verification. Detailed structural generalisability limitations are discussed in Section 4.5.

Four performance indicators were extracted from each simulated cyclic response: peak lateral strength $F_{\max}$, equivalent viscous damping ratio ξ_{eq}, re-centering indicator R_{recenter} and stiffness degradation indicator K_{stiff}. These indicators were treated as separate regression targets rather than combined into a single composite index, because strength recovery, energy dissipation, residual deformation and stiffness degradation describe different aspects of repair performance. The mathematical definitions, units, and model roles of the input variables and output indicators are summarised in Table 3, while the cycle-identification and indicator-extraction procedure is described below. Fig. 4 provides an overview of this database and indicator set by visualising the sample composition, the sampled CFRP repair parameters, the distributions of the four response indicators and the Spearman rank correlations between inputs and outputs. Together with Table 3, these summaries show that the database provides broad parameter coverage and explicit multi-indicator target information for model training.

Table 3: Input variables and output indicators used in the multi-indicator machine-learning framework.

Symbol	Definition	Data Type/Unit	Model Role
Direction	Lateral loading direction of the repaired pier (x or y)	Categorical	Input
DS	Pre-repair damage-state level (DS1-DS5)	Ordinal categorical	Input
t_{CFRP}	Nominal thickness of a single CFRP layer	Continuous/mm	Input
n_{CFRP}	Number of CFRP wrapping layers	Integer/-	Input
f_{CFRP}	Tensile strength of the CFRP sheet	Continuous/MPa	Input
E_{CFRP}	Elastic modulus of the CFRP sheet	Continuous/MPa	Input
h_{CFRP}	CFRP wrapping height measured from the pier base	Continuous/m	Input

(Continued)

Table 3 (continued)

Symbol	Definition	Data Type/Unit	Model Role
$F_{\max}$	Peak lateral strength of the final valid paired cycle, $F_{\max} = \max\left(\lvert F_f^+\rvert, \lvert F_f^-\rvert\right)$, where F_f^+ and F_f^- are the lateral forces at the positive and negative peak-displacement points of the final valid paired cycle.	Continuous/kN	Output
ξ_{eq}	Equivalent viscous damping ratio of the final valid paired cycle, $\xi_{eq} = 100 \times W_D/(4\pi W_S)$, where W_D is the energy dissipated by the paired cycle and W_S is the corresponding reference strain energy.	Continuous/%	Output
R_{recenter}	Branch-averaged re-centering indicator of the final valid paired cycle: $R_{\text{recenter}} = \frac{1}{2}\left[\left(1 - \frac{\lvert\Delta_r^+\rvert}{\lvert\Delta_m^+\rvert}\right) + \left(1 - \frac{\lvert\Delta_r^-\rvert}{\lvert\Delta_m^-\rvert}\right)\right]$, where Δ_r and Δ_m denote the residual and peak displacements of the positive and negative branches.	Continuous/-	Output
K_{stiff}	Branch-averaged stiffness degradation between the first and last valid loop entries: $K_{\text{stiff}} = 100\left\{1 - \frac{1}{2}\left[\frac{K_f^+}{K_0^+} + \frac{K_f^-}{K_0^-}\right]\right\}$, where K_0^+ and K_0^- are the first valid positive- and negative-branch secant stiffnesses, and K_f^+ and K_f^- are their corresponding final valid values.	Continuous/%	Output

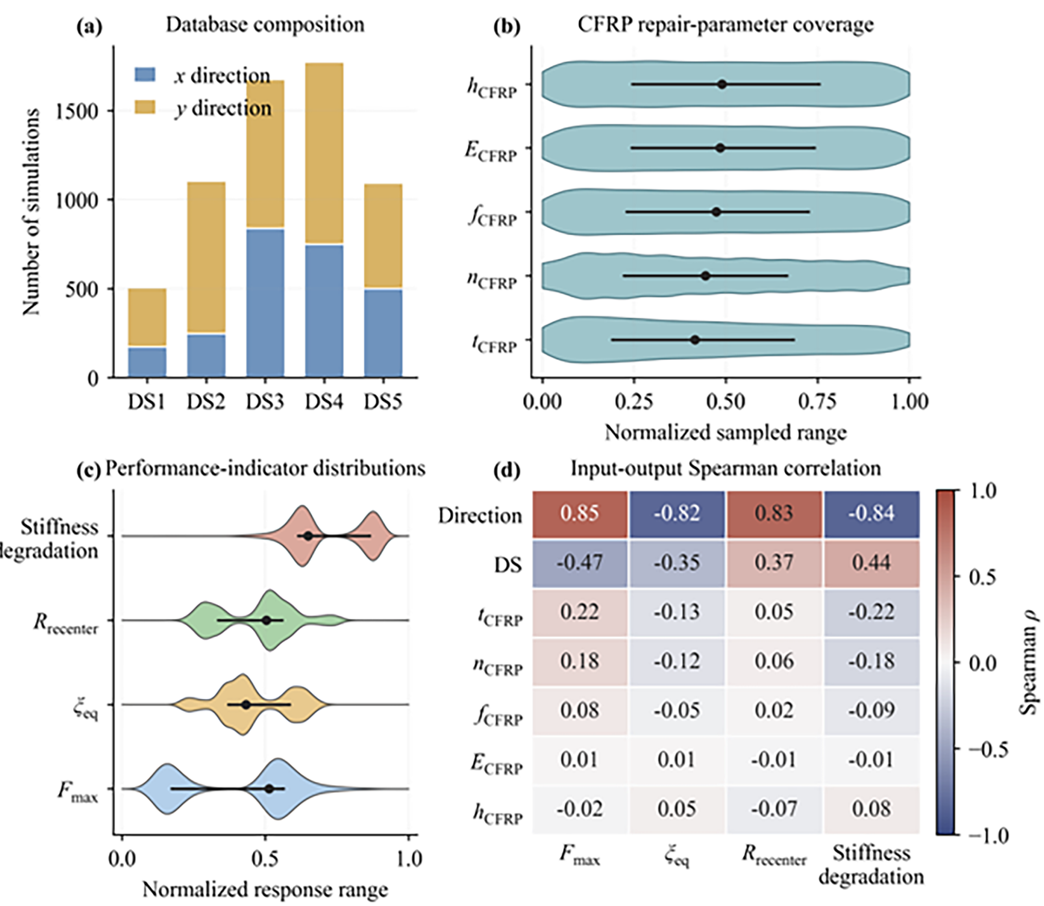

Figure 4: Overview of the FE database: (**a**) sample composition; (**b**) CFRP parameter distributions; (**c**) response-indicator distributions; (**d**) input-output Spearman correlations.

For reproducible indicator extraction, the displacement history was first segmented into positive and negative half-cycles at displacement zero crossings. Half-cycles of opposite signs were paired when the difference between their absolute peak-displacement amplitudes was within a relative tolerance of 2%. Unpaired half-cycles were excluded, and no artificial cycle closure was imposed. The valid paired cycles were ordered by their absolute peak-displacement amplitudes. The final valid paired cycle therefore represented the largest successfully paired displacement excursion available in the response record. The equivalent viscous damping ratio ξ_{eq} and re-centering indicator $R_{recenter}$ were evaluated from this final paired cycle. Peak lateral strength F_{max} was defined as the larger absolute lateral force obtained from the positive and negative branches of the final valid paired cycle. The stiffness degradation indicator K_{stiff} was calculated from the first and last valid secant-stiffness entries for the positive and negative branches. The two branch-specific stiffness-retention ratios were then averaged. Positive and negative branches were evaluated using absolute force and displacement quantities before the scalar values in Table 3 were assigned.

3.3 Performance Indicators and Response-Space Characteristics

Before model training, the four response quantities were examined as a joint response space rather than as isolated data columns. This analysis assessed the degree of statistical coupling among the indicators and whether they should remain separate engineering targets rather than be compressed into a single composite index. It did not constitute an empirical comparison between target-wise and multi-task architectures.

Fig. 5 shows that the response indicators are strongly coupled, but they represent different engineering decision objectives rather than redundant statistics. Peak strength is closely associated with K_{stiff}, and equivalent damping and re-centering occupy another correlated response plane with clear loading-direction dependence. The principal component analysis (PCA) projection also indicates that a large part of the variance is shared among the four indicators. Even so, reducing them to a single scalar would obscure whether a repair scheme improves strength recovery, energy dissipation, residual-deformation control or stiffness-loss mitigation. The observed response-space coupling supports joint interpretation of the four indicators, while their distinct engineering meanings justify retaining them as separate outputs in the present baseline. This choice does not imply statistical independence or demonstrate that target-wise learning is superior to multi-task learning.

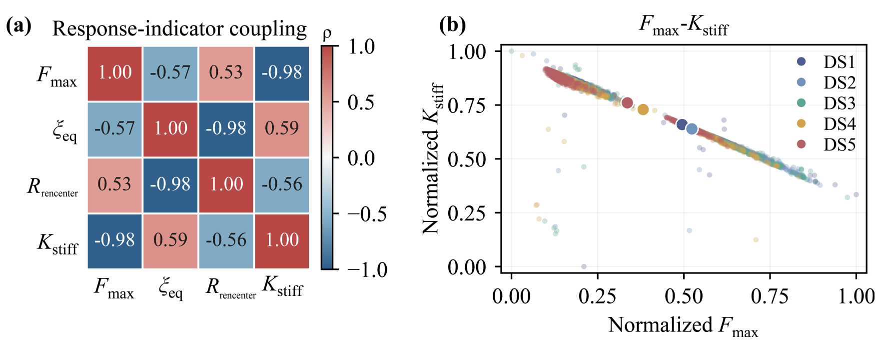

Figure 5: (Continued)

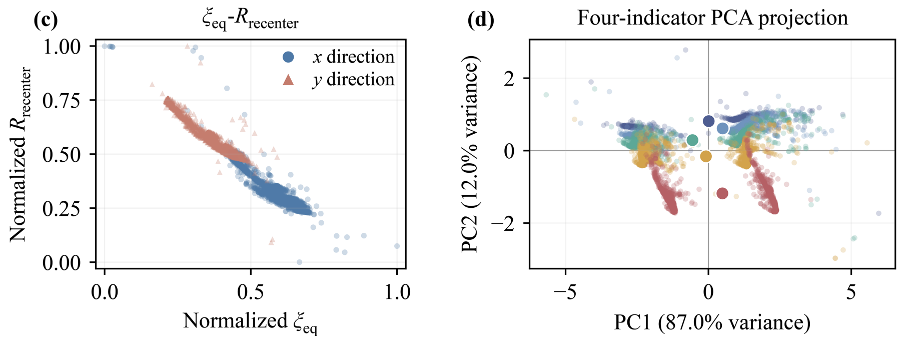

Figure 5: Multi-indicator response-space characteristics: (**a**) target correlations; (**b**) $F_{\max}$–K_{stiff} response plane; (**c**) ξ_{eq}–R_{recenter} response plane; (**d**) principal-component projection.

4 Results and Interpretation

4.1 Comparison of Candidate Models across Indicators

The comparative performance of the seven candidate algorithms is summarised in Fig. 6. Under the predefined target-wise cross-validation protocol, CatBoost was selected for $F_{\max}$, whereas SVR-RBF was selected for ξ_{eq}, R_{recenter} and K_{stiff}. The target-dependent selections motivate the present target-wise baseline, but they do not establish that a shared or multi-task architecture would perform worse because neither architecture was evaluated in this study.

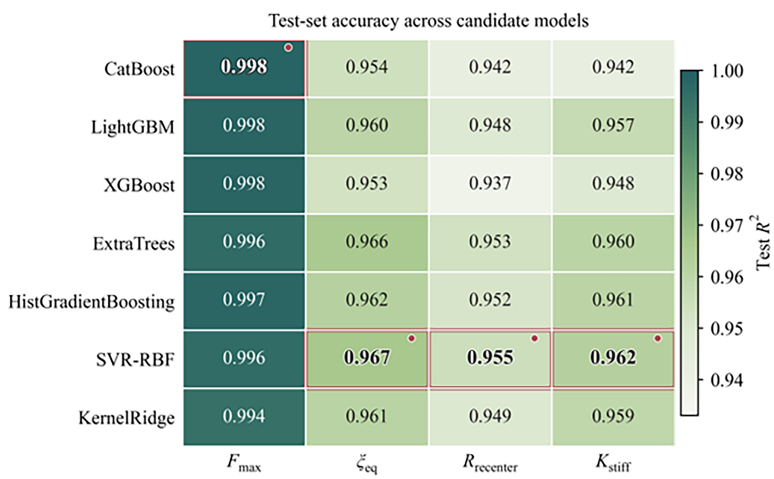

Figure 6: Independent-test R^2 values of the seven candidate models. Red outlines denote the models selected by cross-validation.

The leading model was clear for peak strength. For the deformation- and degradation-related indicators, several alternatives remained competitive: ExtraTrees, HistGradientBoosting, Kernel Ridge, and SVR-RBF all achieved test R^2 values close to or above 0.95 for at least one indicator. This pattern indicates that several model families can approximate these response surfaces effectively under the predefined protocol. Target-wise model selection was therefore retained for the present benchmark, while differences among the top-performing models were treated as marginal where their performance metrics were close.

Because the present comparison used fixed hyperparameter configurations, the resulting model ranking should be interpreted as conditional on the predefined comparison protocol rather than as a universal ranking of the seven algorithms. Systematic hyperparameter optimization could change the ordering of models with closely comparable cross-validation performance, particularly for ξ_{eq}, $R_{recenter}$, and K_{stiff}. Future work should examine the robustness of the model ranking using nested hyperparameter optimization and repeated data splitting.

The correlations among the four response indicators make multi-output or multi-task learning a relevant alternative. Recent structural-engineering research has demonstrated that a multi-task surrogate trained on finite-element data can simultaneously predict heterogeneous bridge responses, including nodal displacements and element bending moments, for cable-stayed bridge optimisation [30]. However, the present study did not compare target-wise and multi-task architectures. A controlled comparison would require output normalisation, task-loss weighting, selection of the shared representation, assessment of possible negative transfer, and evaluation under the same data split and tuning budget. Accordingly, the target-wise strategy is used here as a transparent baseline that preserves the four indicators as separate engineering decision quantities, rather than as evidence that target-wise learning is intrinsically superior to multi-task learning.

4.2 Prediction Performance of Selected Indicator-Specific Models

After target-wise model selection, the selected indicator-specific models were tested on the independent subset. Fig. 7 compares the predicted and simulated values for the four seismic-performance indicators. The points concentrate around the 1:1 reference line in all panels, showing that the models captured the dominant nonlinear relationships among damage state, CFRP repair parameters, and structural response.

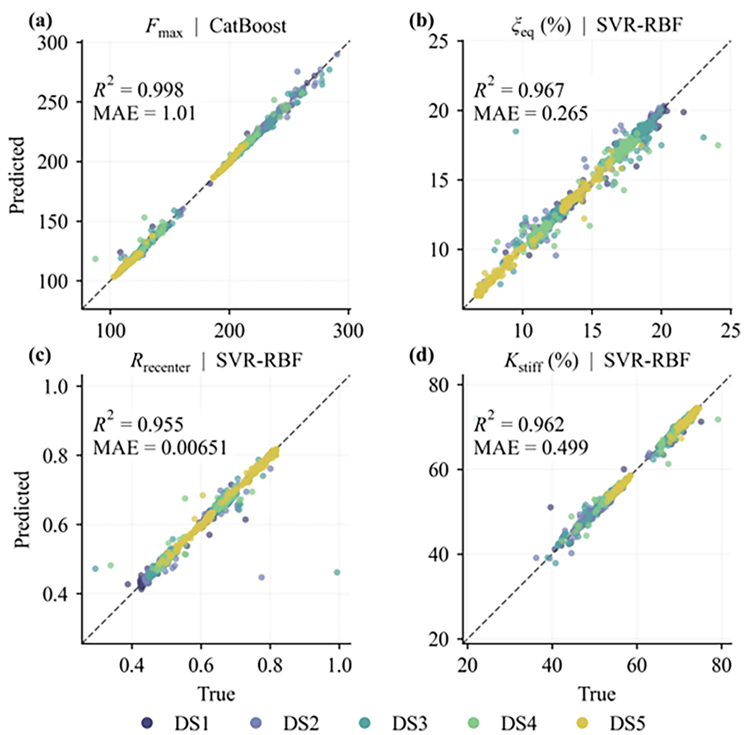

Figure 7: Independent-test predictions for (**a**) F_{max}; (**b**) ξ_{eq}; (**c**) $R_{recenter}$; and (**d**) K_{stiff}. Colours denote damage states.

Peak lateral strength was predicted most accurately. CatBoost achieved a test R^2 of 0.9981, an RMSE of 2.103 kN, an MAE of 1.009 kN, and a MAPE of 0.605% relative to the FE-generated labels. The three hysteresis-shape-related indicators also showed high numerical accuracy with SVR-RBF: the test R^2 values were 0.9666 for ξ_{eq}, 0.9548 for $R_{recenter}$, and 0.9625 for K_{stiff}. Their corresponding MAPEs were 2.060%, 1.107%, and 1.010%, respectively. These results match the summary reported in Fig. 3c and show that the four selected target-specific models can interpolate the sampled FE response surface with high fidelity.

The reported R^2, RMSE, MAE and MAPE values quantify agreement with the FE-generated labels and therefore represent surrogate interpolation error rather than direct experimental or field prediction accuracy. This numerical error should be distinguished from the physical-modelling uncertainty of the underlying FE model. Across the available validation comparisons, the absolute FE-to-experiment peak-load differences ranged from 1.4% to approximately 20.0%. This range represents observed peak-load discrepancies rather than a probabilistic uncertainty interval and cannot be assigned uniformly to ξ_{eq}, $R_{recenter}$ and K_{stiff}. When a predicted response lies close to an engineering acceptance or repair-decision threshold, the corresponding scheme should therefore be re-evaluated using the underlying FE model and, where practicable, additional experimental evidence.

Grouped error diagnostics were also used to check whether the prediction errors were concentrated in particular damage states or loading directions. Because the train-test split was stratified by damage state and loading direction, the grouped error analysis further examined whether the selected models remained stable across the main categorical sources of response variation. This analysis was used to evaluate damage-state sensitivity and direction-dependent prediction stability, rather than only global average accuracy. Fig. 8 reports MAPE values grouped by DS and by loading direction, complementing the global test metrics in Fig. 7 by showing local reliability across the sampled repairable damage domain.

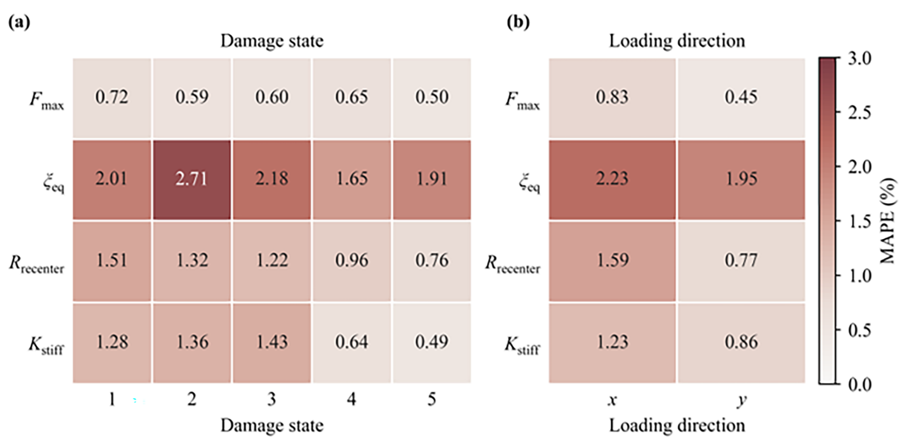

Figure 8: Grouped error diagnostics of the selected indicator-specific models: (**a**) MAPE grouped by damage state; (**b**) MAPE grouped by loading direction.

The grouped errors remained low across all subsets. For peak strength, the DS-based MAPE ranged from 0.499% to 0.722%. For ξ_{eq}, the largest DS-based MAPE occurred at DS2 (2.709%), while $R_{recenter}$ and K_{stiff} reached their largest DS-based MAPEs at DS1 (1.51%) and DS3 (1.43%), respectively. Direction-based errors were generally higher in the x direction than in the y direction, particularly for $R_{recenter}$ and K_{stiff}. Although the grouped MAPEs remained low, the subgroup R^2 values were lower for the x-direction predictions of $R_{recenter}$ (0.714) and K_{stiff} (0.372). The grouped results therefore indicate small absolute percentage errors, but not uniformly high variance-explanation accuracy across all direction–indicator combinations.

4.3 Interpretability and Mechanical Consistency

A model-agnostic Shapley additive explanations (SHAP) analysis was conducted using 180 cases sampled from the independent test subset with stratification by loading direction and damage state [17,18]. A disjoint set of 80 independent-test cases was used as the background distribution. The same explanation and background cases were used for all four selected indicator-specific models. SHAP values were computed for all seven input variables to evaluate both the magnitude and direction of their contributions.

Fig. 9 presents the SHAP distributions for the four predicted performance indicators. The feature rows follow a common order across all four panels to facilitate cross-target comparison and should not be interpreted as separate target-specific importance rankings. Each dot represents one of the 180 explanation cases, and its horizontal position gives the corresponding SHAP contribution. Colour denotes the relative feature value; for categorical variables, it represents the encoded category rather than a continuous physical magnitude.

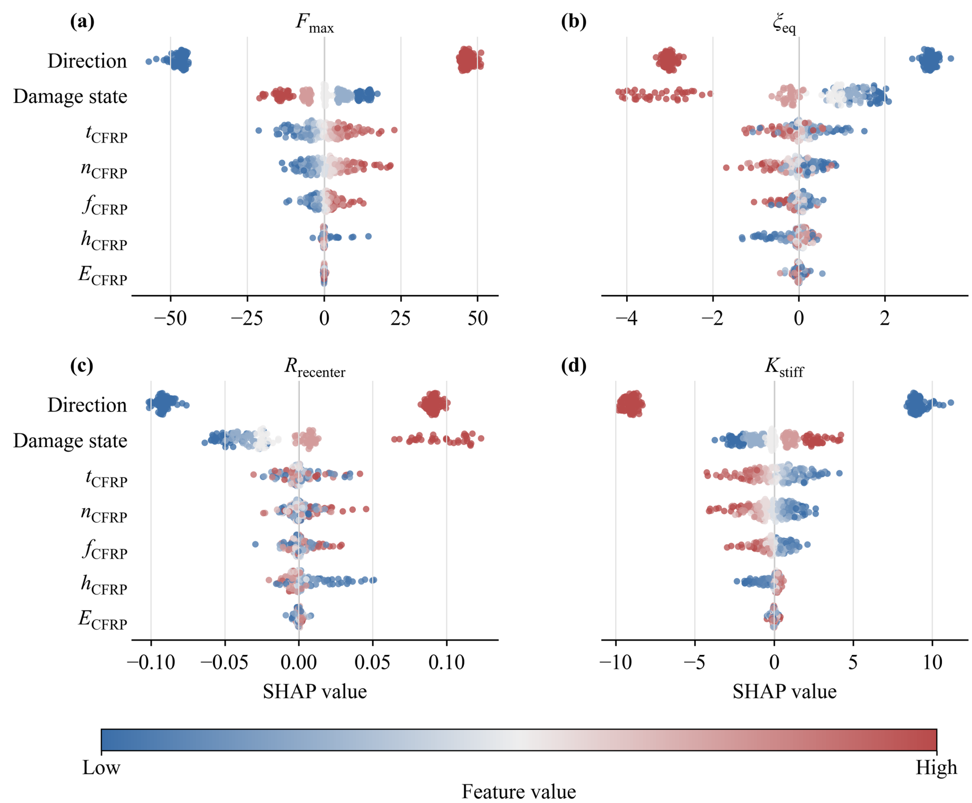

Figure 9: SHAP summary plots for the selected models: (**a**) F_{max}; (**b**) ξ_{eq}; (**c**) $R_{recenter}$; and (**d**) K_{stiff}. The panels use the same 180 stratified explanation cases and a common feature-row order for cross-panel comparison; row position does not represent a target-specific importance ranking.

The SHAP patterns show that loading direction and damage state provide substantial explanatory information for several response indicators. The CFRP repair parameters then contribute in an output-specific manner. Thickness, layer number, tensile strength, elastic modulus, and repair height do not have identical effects on strength, damping, re-centering, and stiffness degradation. This behaviour is consistent with the mechanics of repaired hollow piers: damage state and loading axis define the initial response regime, while the CFRP configuration modifies confinement and cyclic-degradation behaviour within that regime.

For K_{stiff}, the audited mean absolute SHAP magnitudes were 9.112 for Direction, 1.512 for DS, 1.239 for t_{CFRP}, and 1.083 for n_{CFRP}. Thus, the final results place DS above n_{CFRP} rather than the reverse. Mechanically, DS defines the pre-repair stiffness regime through the damage-dependent reductions in the elastic moduli of concrete and reinforcement listed in Table 1 [23,24]. By contrast, n_{CFRP} modifies the repaired response through its influence on CFRP confinement but does not remove the pre-existing concrete cracking or reinforcement damage represented by DS. Direction had the largest contribution, which is consistent with the different stiffness and hysteretic-response characteristics of the round-ended hollow section along its two principal axes. These SHAP values describe model attribution within the sampled FE domain and should not be interpreted as a universal causal ranking for CFRP-repaired reinforced-concrete piers.

4.4 Influence of CFRP Repair Parameters on Performance Indicators

The preceding SHAP analysis identifies which variables contribute to the selected models, but it does not directly show how practical CFRP repair parameters change the predicted performance indicators. To examine these effects more completely, partial-dependence plots (PDPs) were generated for all five CFRP variables: t_{CFRP}, n_{CFRP}, f_{CFRP}, E_{CFRP}, and h_{CFRP}. The independent-test feature distribution was used as the background domain. The resulting curves therefore describe learned trends within the sampled repairable-response domain rather than unconstrained design rules.

Fig. 10a summarizes the effect amplitude of each CFRP parameter as a percentage of the corresponding target-response range. The thickness t_{CFRP} and layer number n_{CFRP} give the largest CFRP-parameter effects for F_{max} and K_{stiff}, while f_{CFRP} has a secondary but visible contribution. The elastic modulus E_{CFRP} produces only small changes in all four targets within the sampled range. The repair height h_{CFRP} is less influential for F_{max} than t_{CFRP} or n_{CFRP}, but it has clearer effects on ξ_{eq}, $R_{recenter}$, and K_{stiff}.

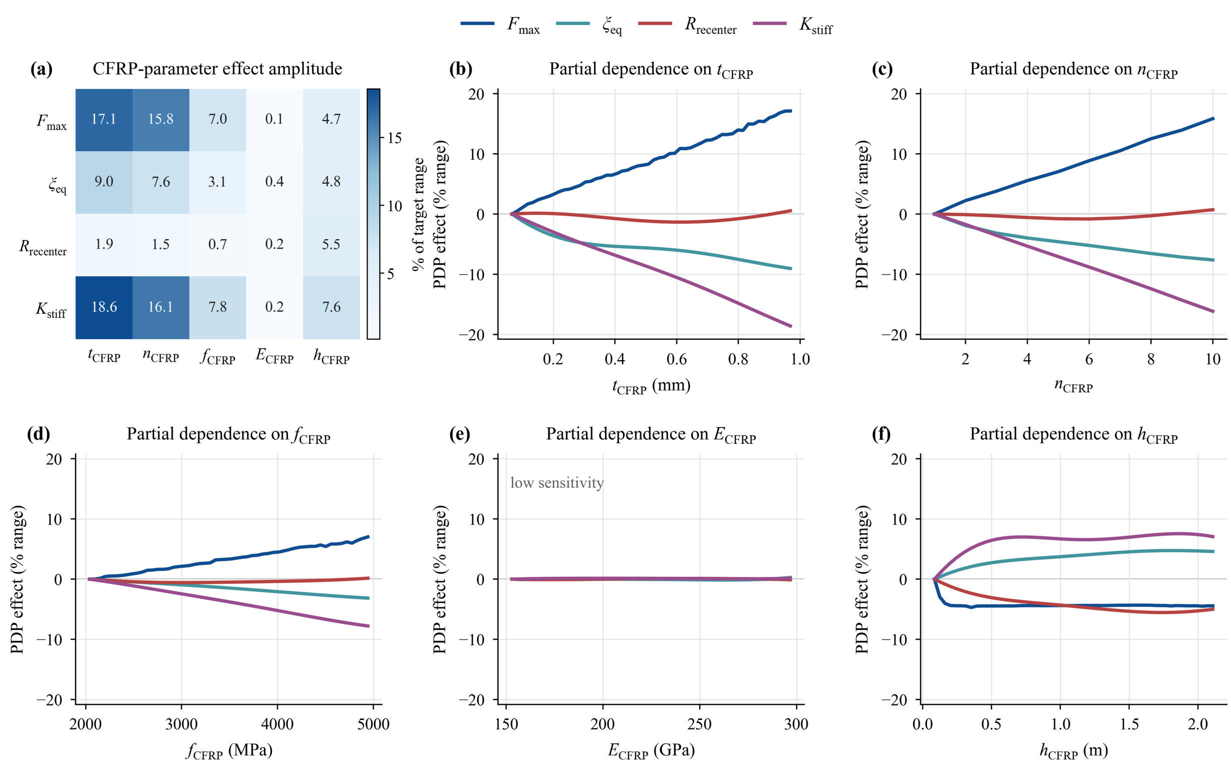

Figure 10: Partial-dependence effects of CFRP parameters: (**a**) relative effect amplitudes; (**b–f**) centred curves for t_{CFRP}, n_{CFRP}, f_{CFRP}, E_{CFRP}, and h_{CFRP}.

The PDPs in Fig. 10b–f show that the five CFRP parameters do not act in the same direction for all indicators. Increasing t_{CFRP}, n_{CFRP}, and f_{CFRP} generally raises the predicted $F_{\max}$, whereas ξ_{eq} and K_{stiff} move in the opposite direction over much of the same range. The response to h_{CFRP} is different: it changes the hysteretic indicators more strongly than $F_{\max}$ and introduces a non-monotonic trend for R_{recenter}. The E_{CFRP} curves remain nearly horizontal at the shared scale, which is consistent with the low effect amplitudes in Fig. 10a. These patterns indicate a practical trade-off: parameter choices that improve peak strength do not necessarily optimize all hysteretic-performance indicators. Multi-indicator screening is therefore preferable to strength-only repair selection.

4.5 Limitations and Generalisability

The present surrogate framework is configuration-specific. All 6152 retained cases were generated from one round-ended hollow pier prototype. The geometry, hollow-section characteristics, axial-load condition, reinforcement configuration, and base concrete and reinforcement properties were fixed. Only loading direction, pre-repair damage state, and the five CFRP repair variables were varied. Consequently, the reported metrics quantify interpolation within this numerical design space. They do not establish comparable accuracy for other pier heights, aspect ratios, hollow ratios, axial-load ratios, reinforcement ratios, or structural configurations.

Experimental anchoring is limited to four 1:10-scale specimens subjected to uniaxial reversed cyclic loading along the x and y principal directions [23]. The wider CFRP parameter ranges in the database are numerical extensions of the validated FE formulation rather than independently validated experimental configurations. Other pier geometries, arbitrary oblique loading, simultaneous biaxial loading, and structural systems not represented in the database should therefore be treated as out of domain. The boundary-zone guidance in Section 3.2 is an operational screening rule and does not establish structural extrapolation capability. Although the CFRP tensile strength and elastic modulus were varied parametrically, uncertainty in their field values, damage-state identification, repair workmanship and quality, and construction tolerances was not modelled explicitly and would require separate treatment in field applications.

Extension to other pier configurations requires experimentally anchored FE datasets that explicitly vary geometry, hollow ratio, axial-load ratio, reinforcement configuration, material properties, and loading path. Configuration-level holdout validation should also keep entire pier configurations or loading conditions outside the training data. Until such evidence is available, cross-pier applications require case-specific FE analysis and, where practicable, additional experimental validation before the surrogate is used for optimisation, design, or performance certification.

5 Conclusions

This study developed a finite-element database anchored to test results reported in the authors' previous study and a target-wise machine-learning framework for predicting the seismic performance of earthquake-damaged CFRP-repaired hollow bridge piers. The framework links test-validated cyclic simulations with indicator-specific surrogate models. It therefore preserves the distinct mechanical roles of strength recovery, energy dissipation, residual-deformation control and stiffness degradation.

(1) The OpenSeesPy model reproduced the principal hysteretic responses and peak lateral strengths of the unrepaired and CFRP-repaired specimens reported in the authors' previous study [19]. Across the positive- and negative-branch peak loads, the absolute relative differences between the FE predictions and experimental measurements ranged from 1.4% to approximately 20.0%. The model was subsequently used for repair-parameter trend analysis and FE-response database generation, while these discrepancies were retained as an explicit source of physical-modelling uncertainty. Because the validation tests involved

uniaxial reversed cyclic loading along only the two principal directions, the results do not establish model accuracy under arbitrary oblique or simultaneous biaxial loading.

(2) The test-validated FE model generated 6152 converged repair cases across five damage states and two loading directions. All retained cases nevertheless shared the same prototype geometry, axial-load condition, and reinforcement configuration. The larger database therefore expands the sampled parameter combinations within one structural configuration but does not demonstrate cross-pier generalisability. The database also covered broad ranges of CFRP thickness, layer number, tensile strength, elastic modulus and repair height as a numerical parametric extension beyond the repair configuration tested in the authors' previous study. Response-space analysis showed that the four indicators are strongly coupled but correspond to different engineering decision objectives. This finding supports a multi-indicator prediction strategy rather than a single composite repair index.

(3) Target-wise model selection showed that different seismic-performance indicators favoured different model forms. CatBoost was selected for peak lateral strength, whereas SVR-RBF was selected for equivalent damping, re-centering, and stiffness degradation under the predefined comparison protocol. Several alternative models achieved closely comparable accuracy for the latter three indicators, indicating that the selected predictor bank is protocol-specific rather than universally optimal. On the independent test set, the four selected models achieved R^2 values of 0.9981 for F_{max}, 0.9666 for ξ_{eq}, 0.9548 for R_{recenter} and 0.9625 for K_{stiff} relative to the FE-generated labels. These results show that the surrogate models captured the dominant nonlinear relationships within the sampled numerical response space. However, these accuracy values represent surrogate interpolation fidelity relative to FE-generated labels, not independent physical prediction accuracy for actual repaired bridge piers.

(4) The SHAP and partial-dependence analyses provided mechanically interpretable trends. Damage state and loading direction strongly affected the predicted responses. CFRP thickness, layer number, tensile strength, elastic modulus and repair height then contributed in indicator-specific ways. Increasing CFRP thickness, layer number and tensile strength generally raised the predicted peak strength. However, these changes did not improve all hysteretic indicators at the same time. Repair height affected damping, re-centering and stiffness degradation more clearly than peak strength. These trade-offs highlight the need for multi-indicator screening when selecting CFRP repair schemes.

Overall, the proposed framework provides a rapid and interpretable tool for preliminary assessment of CFRP-repaired hollow bridge piers within the numerical response domain of the investigated prototype. Because the surrogate models were trained on FE-generated labels, they should be interpreted as interpolation and screening tools rather than substitutes for experimental validation or field-level repair certification. Applications to different pier geometries, axial-load ratios, reinforcement configurations, or loading paths should be treated as out of domain and require case-specific FE analysis and additional experimental evidence. Future work should expand the experimentally anchored database to additional pier geometries, axial-load ratios, reinforcement configurations, and loading paths, compare target-specific and multi-task architectures under a common evaluation protocol, and establish uncertainty-aware out-of-domain checks before coupling the surrogate with repair-scheme optimisation.

Acknowledgement: Numerical computations in this study were performed using the computing resources provided by the Hefei Advanced Computing Center.

Funding Statement: This research was financially supported by the National Natural Science Foundation of China (U2368210, 52378209), the China Railway Group Limited Major Project (2023-Major-20), the Hunan Province Science and Technology Project Huxiang Young Talents Program (2023RC3057), and the University-Industry Joint Innovation Project of Central South University (2025XOLH033).

Author Contributions: The authors confirm contribution to the paper as follows: Conceptualization, Liqiang Jiang; methodology, Song Tan; software, Song Tan; validation, Song Tan; formal analysis, Song Tan; investigation, Liqiang Jiang; resources, Liqiang Jiang; data curation, Wei Guo; writing—original draft preparation, Song Tan; writing—review and editing, Liqiang Jiang; visualization, Wei Guo; supervision, Fengqi Guo; project administration, Wei Guo; funding acquisition, Lizhong Jiang, Fengqi Guo and Liqiang Jiang. All authors reviewed and approved the final version of the manuscript.

Availability of Data and Materials: The finite element simulation database, model-performance summaries, and trained estimator bundles generated in this study are available from the corresponding author, Liqiang Jiang, upon reasonable request for academic verification and reuse within the sampled numerical modelling domain.

Ethics Approval: Not applicable. This study did not involve human participants or animals.

Conflicts of Interest: The authors declare no conflicts of interest.

References

1. He R, Yang Y, Sneed LH. Seismic repair of reinforced concrete bridge columns: review of research findings. J Bridge Eng. 2015;20(12):04015015. doi:10.1061/(asce)be.1943-5592.0000760.
2. Tazarv M, Won K, Jang Y, Hart K, Greeneway E. Post-earthquake serviceability assessment of standard RC bridge columns using computer vision and seismic analyses. Eng Struct. 2022;272:115002. doi:10.1016/j.engstruct.2022.115002.
3. Kong Z, Jiang L, Liu X, Jiang L, Wei B, He C. System-level post-earthquake functional recovery function and seismic resilience assessment of high-speed railway track-bridge systems. Eng Struct. 2026;354:122430. doi:10.1016/j.engstruct.2026.122430.
4. Kang Z, Jiang L, Liu J, Jiang L. System-level recovery assessment of high-speed railway bridges with CFRP-repaired RC hollow piers under near-fault ground motions. Eng Struct. 2026;357:122532. doi:10.1016/j.engstruct.2026.122532.
5. Liang X, Shao C, Han Q. Seismic performance of round-end hollow RC tall bridge piers considering to higher-order vibration mode effect. Adv Bridge Eng. 2024;5(1):35. doi:10.1186/s43251-024-00146-0.
6. Shao C, Wei W, Wu S, Qi Q, Wang C. Experimental investigation on plastic hinge length of RC round-ended hollow columns with a variable section. Eng Struct. 2023;290:116358. doi:10.1016/j.engstruct.2023.116358.
7. He Y, Cai G, Xie C, Malla PB, Li Y, Si Larbi A. Seismic experimental research on damaged resilient reinforced concrete columns retrofitted by FRP sheets. Eng Struct. 2025;332:120119. doi:10.1016/j.engstruct.2025.120119.
8. Lei S, Wu F, Liu L, Chen X, Peng B. Seismic repair of damaged columns with CFRP bars and sheets. Structures. 2025;81:110357. doi:10.1016/j.istruc.2025.110357.
9. Rodrigues H, Furtado A, Arêde A. Experimental evaluation of energy dissipation and viscous damping of repaired and strengthened RC columns with CFRP jacketing under biaxial load. Eng Struct. 2017;145:162–75. doi:10.1016/j.engstruct.2017.05.021.
10. Wang D, Wang Z, Yu T, Li H. Seismic performance of CFRP-retrofitted large-scale rectangular RC columns under lateral loading in different directions. Compos Struct. 2018;192:475–88. doi:10.1016/j.compstruct.2018.03.029.
11. Zhu F, Zhang M, Zhang D, Wang D, Wang Z, Zhang Y. Seismic behavior of FRP-retrofitted rectangular RC columns subjected to oblique horizontal earthquake actions. Constr Build Mater. 2025;482:141737. doi:10.1016/j.conbuildmat.2025.141737.
12. Hu S, Guo T, Alam MS, Koetaka Y, Ghafoori E, Karavasilis TL. Machine learning in earthquake engineering: a review on recent progress and future trends in seismic performance evaluation and design. Eng Struct. 2025;340:120721. doi:10.1016/j.engstruct.2025.120721.
13. Yazdanpanah O, Chang M, Ali Bakhshi E. Attention-based hybrid convolutional-long short-term memory network for bridge pier hysteresis and backbone curves prediction. Integr Comput Aided Eng. 2025;32(2):176–95. doi:10.1177/10692509241301240.

14. Yuan C, Fang X, Li Z, Kong Q, Chen W, Hao H. A novel BWBN-integrated physics-informed neural network for advanced hysteretic modeling of RC structures under cyclic loads. Eng Struct. 2025;345:121542. doi:10.1016/j.engstruct.2025.121542.
15. Todorov B, Muntasir Billah A. Machine learning driven seismic performance limit state identification for performance-based seismic design of bridge piers. Eng Struct. 2022;255:113919. doi:10.1016/j.engstruct.2022.113919.
16. Mo R, Chen L, Chen Y, Xiong C, Zhang C, Chen Z, et al. Prediction and correlations estimation of seismic capacities of pier columns: extended Gaussian process regression models. Struct Saf. 2024;109:102457. doi:10.1016/j.strusafe.2024.102457.
17. Gharagoz MM, Noureldin M, Kim J. Explainable machine learning (XML) framework for seismic assessment of structures using Extreme Gradient Boosting (XGBoost). Eng Struct. 2025;327:119621. doi:10.1016/j.engstruct.2025.119621.
18. Lundberg SM, Lee SI. A unified approach to interpreting model predictions. Adv Neural Inf Process Syst. 2017;30:4765–74. doi:10.48550/arxiv.1705.07874.
19. Tan S, Jiang L, Jiang L, Zhou W, Liu J, Guo F. Effects of CFRP-repaired round-end RC hollow piers on postearthquake recovery of high-speed railway track-bridge systems. J Bridge Eng. 2026;31(9):04026054. doi:10.1061/jbenf2.beeng-7962.
20. McKenna F. OpenSees: a framework for earthquake engineering simulation. Comput Sci Eng. 2011;13(4):58–66. doi:10.1109/MCSE.2011.66.
21. Zhu M, McKenna F, Scott MH. OpenSeesPy: Python library for the OpenSees finite element framework. SoftwareX. 2018;7(1):6–11. doi:10.1016/j.softx.2017.10.009.
22. Scott MH, Fenves GL. Plastic hinge integration methods for force-based beam-column elements. J Struct Eng. 2006;132(2):244–52. doi:10.1061/(asce)0733-9445(2006)132:2(244).
23. Vosooghi A, Saiidi MS. Design guidelines for rapid repair of earthquake-damaged circular RC bridge columns using CFRP. J Bridge Eng. 2013;18(9):827–36. doi:10.1061/(asce)be.1943-5592.0000426.
24. Sun Z, Guan L, Zhao T, Si B, Niu J. Analysis model and seismic behavior of repaired RC bridge piers after earthquakes by using CFRP. J Basic Sci Eng. 2020;28(4):878–89. doi:10.16058/j.issn.1005-0930.2020.04.011.
25. Vosooghi A, Saiidi MS. Shake-table studies of repaired reinforced concrete bridge columns using carbon fiber-reinforced polymer fabrics. ACI Struct J. 2013;110(1):105–14. doi:10.14359/51684334.
26. Braga F, Gigliotti R, Laterza M. Analytical stress-strain relationship for concrete confined by steel stirrups and/or FRP jackets. J Struct Eng. 2006;132(9):1402–16. doi:10.1061/(asce)0733-9445(2006)132:9(1402).
27. Pedregosa F, Varoquaux G, Gramfort A, Michel V, Thirion B, Grisel O, et al. Scikit-learn: machine learning in Python. J Mach Learn Res. 2011;12:2825–30. doi:10.48550/arxiv.1201.0490.
28. Hancock JT, Khoshgoftaar TM. CatBoost for big data: an interdisciplinary review. J Big Data. 2020;7(1):94. doi:10.1186/s40537-020-00369-8.
29. Chen T, Guestrin C. XGBoost: a scalable tree boosting system. In: Proceedings of the 22nd ACM SIGKDD International Conference on Knowledge Discovery and Data Mining; 2016 Aug 13–19; San Francisco, CA, USA. New York, NY, USA: ACM; 2016. p. 785–94. doi:10.1145/2939672.2939785.
30. Lei Y, Liu Q, Wu X, Zhu S, Zhao J, Ren X. A novel multi-task graph neural network model for cable force optimization in cable-stayed bridges. Eng Struct. 2025;345:121468. doi:10.1016/j.engstruct.2025.121468.